Mechanics of Materials 216 (2026) 105648

Contents lists available at ScienceDirect

Mechanics of Materials

journal homepage: www.elsevier.com/locate/mecmat

Research paper

Fracture mechanics of open-porous materials: A Voronoi-based approach

Rajesh Chandrasekaran [a,*], Mikhail Itskov [a], Ameya Rege [b]

[a] Department of Continuum Mechanics, RWTH Aachen University, Eilfschornsteinstr. 18, Aachen, 52062, Germany
[b] Department of Mechanics of Solids, Surfaces & Systems, University of Twente, PO Box 217, 7500 AE, Enschede, The Netherlands

ARTICLE INFO

Invited Editor Ghatu Subhash

Keywords:
Fracture mechanics
Open-porous material
Solid fraction
Fracture strength
Fracture toughness
Energy release rate
Crack depth
Crack angle

ABSTRACT

The fracture behavior of open-porous materials is governed by a complex interplay between microstructural architecture and crack propagation mechanisms, necessitating systematic investigation to ensure their reliable use in structural, biomedical, and thermal insulation applications. Quantifying fracture toughness and strain energy release rates is essential for optimizing mechanical stability under stress. This study presents a computational framework based on Laguerre-Voronoi tessellation to model the intricate cellular architecture of open-porous solids. Under tensile loading, the model reproduces the classical scaling relations proposed by Maiti, Gibson, and Ashby. The effective elastic modulus exhibits a nearly quadratic dependence on the solid fraction, while the normalized fracture behavior follows a square-root function of the solid fraction. The model prediction for the normalized fracture toughness shows good agreement with experimental data reported in the literature. This consistency confirms the capability of Voronoi-based microstructures to capture established power laws, while also revealing deviations associated with pronounced heterogeneity. Subsequently, the key microstructural parameters, including solid fraction, pore size and pore-wall thickness, as well as the macroscopic crack geometric features, such as crack depth-to-height ratio and crack orientation, are systematically varied to assess their influence on fracture resistance. The results reveal critical dependence of crack propagation and energy dissipation on microstructural features, demonstrating how porosity and pore size distribution can be tuned to tailor the mechanical response. These findings contribute to a deeper understanding of fracture mechanics in porous systems and underscore the need for microstructure-informed material design to enhance mechanical performance.

1. Introduction

Open-porous materials, defined by a continuous solid framework interwoven with interconnected voids, represent a distinct class of multifunctional materials with outstanding performance characteristics. Their high porosity and interconnected pore architecture enable efficient fluid flow, mass transport, and energy dissipation, making them highly suitable for a wide range of applications. Owing to their favorable combination of mechanical resilience, thermal insulation, and transport properties, these materials find broad use in sectors such as energy storage, filtration, aerospace, automotive, biomedical engineering, and construction. Notable examples include metallic and polymeric foams, which exhibit low density, high specific strength, and excellent energy absorption capabilities (Ensarioglu et al., 2022). Polymeric foams, such as polyurethane and polyvinyl chloride, are widely employed as core materials in sandwich structures for the automotive and aerospace sectors, providing impact resistance and energy absorption in crash scenarios (Kabir et al., 2006). Ceramic foams, with their high-temperature stability and chemical resistance, are pivotal in filtration processes and catalytic substrates (Twigg and Richardson, 2002). Additionally, porous materials offer remarkable thermal and acoustic insulation properties, making them vital for construction and refrigeration applications (Rashidi et al., 2018). In biomedical applications, porous scaffolds fabricated from biodegradable polymers or ceramics have been utilized to mimic the extracellular matrix, promoting cell growth and tissue regeneration (Freyman et al., 2001). At the nanoscale, materials such as aerogels and zeolites exhibit extraordinary properties, including ultralow density, high surface area, and excellent thermal insulation. Among many applications, aerogels are predominantly used as lightweight insulation in aerospace applications (Khan et al., 2024), while zeolites are critical components in catalysis and molecular sieving processes (Kianfar and Mahler, 2020; Zhao et al., 2018).

Despite their broad range of applications and advances in synthesis and characterization techniques, the mechanical and fracture

* Corresponding author.
E-mail addresses: chandrasekaran@km.rwth-aachen.de (R. Chandrasekaran), itskov@km.rwth-aachen.de (M. Itskov), ameya.rege@utwente.nl (A. Rege).
URLs: https://www.km.rwth-aachen.de (M. Itskov), https://people.utwente.nl/ameya.rege (A. Rege).

https://doi.org/10.1016/j.mechmat.2026.105648
Received 2 August 2025; Received in revised form 11 December 2025; Accepted 20 February 2026
Available online 23 February 2026
0167-6636/© 2026 The Authors. Published by Elsevier Ltd. This is an open access article under the CC BY license (http://creativecommons.org/licenses/by/4.0/).

Nomenclature

ϕ	Porosity
ϕ_s	Solid fraction
ρ	Envelope density
ρ_s	Skeletal density
d	Pore-wall thickness
l	Pore-wall length
E	Young's modulus of bulk material
E_s	Young's modulus of pore-wall material
$P(\bullet)$	Pore-size distribution
n	Total number of pore-width intervals
D	Pore-width
$f_1(\bullet)$	Volume of pores (explicit function)
$f_2(\bullet)$	Type of distribution (explicit function)
a	Crack depth
α	Crack angle
K_{IC}	Fracture toughness (Mode I)
G	Strain energy release rate
$\frac{E}{E_s}$	Relative elastic/Young modulus
K_I	Stress intensity factor (Mode I)
σ_f	Macroscopic critical strain at fracture
σ_f	Macroscopic critical stress at fracture
σ_{fs}	Fracture strength of pore-wall material
$\frac{K_{IC}}{\sigma_{fs}\sqrt{\pi l}}$	Normalized fracture toughness
γ_s	Surface energy
F_I	Geometric correction factor (Mode I)
F_W	Width factor
F_N	Crack shape factor
λ_1	Notch singularity exponent
$\frac{a}{h}$	Crack depth-to-length ratio
C_1, n	Constants for elastic moduls–density scaling
c, m	Constants for fracture toughness–density scaling
c_1, m_1	Constants for strain–energy release rate–density scaling

behavior of open-porous materials remains a subject of ongoing investigation. The ability to tailor these materials for specific performance requirements – such as high mechanical strength, low weight, fracture toughness, and thermal efficiency – relies critically on precise control of their microstructural features during fabrication. Key structural parameters, including pore size, shape, distribution, and wall thickness, play a decisive role in governing both functional and mechanical properties. For instance, in filtration and separation systems, pore size directly influences selectivity, whereas in load-bearing applications, the connectivity and thickness of pore walls predominantly determine stiffness, strength, and fracture resistance. In cellular-like materials, the deformation fields differ substantially from those in homogeneous solids due to their intrinsic structural complexity introduced by an interconnected pore network. This architecture alters the internal force distribution and profoundly affects the mechanical behavior under tensile and compressive loading. The lower relative density of the microstructure further amplifies deviations from classical homogeneous continuum behavior, owing to its stochastic nature (Chen et al., 2022). Therefore, a fundamental understanding of how microstructural characteristics, such as porosity, pore size distribution (PSD), and wall geometry, influence macroscopic mechanical responses is essential for the rational design and optimization of open-porous materials across diverse application domains.

Various micromechanical models have been developed to predict the mechanical behavior of cellular-like materials and to analyze the deformation and failure mechanisms of pore walls under applied loads. These models provide critical insights into key aspects, such as the dependence of effective elastic stiffness and failure properties on relative density and the failure modes of individual cells (Ashby and Gibson, 1997). For low-density open-porous materials, the pore-wall geometry, such as the cross-section diameter (d) and length (l), can be correlated to the relative density (ρ/ρ_s) using the following relation (Gibson and Ashby, 1982; Oliveira, 2005),

$$\frac{\rho}{\rho_s} \cong \left(\frac{d}{l}\right)^2, \tag{1}$$

where ρ and ρ_s denote the envelope and skeletal densities, respectively. The relative density is also expressed in terms of the solid fraction (ϕ_s), i.e., $\rho/\rho_s = \phi_s = 1 - \phi$, where ϕ represents the porosity.

The mechanical behavior of porous materials under tension and compression has been systematically described by Gibson and Ashby (1982) using a foundational scaling relationship, correlating the relative Young modulus (E/E_s) to the relative density, expressed as

$$\frac{E}{E_s} = C_1\left(\frac{\rho}{\rho_s}\right)^n, \quad \text{with} \quad n = 2, \tag{2}$$

where E and E_s denote the Young's modulus of the porous material and the solid (pore-wall) material, respectively, and C_1 denotes a dimensionless constant that depends on the microstructural geometry, including the topology and regularity of the pore network. For an idealized uniform pore structure, $C_1 = 1$. The underlying physics is that the relative density scales with the cross-sectional area, while the stiffness scales with the second moment of the cross-sectional area, leading to the quadratic dependence of the relative Young's modulus on the solid fraction/relative density. Recently, a similar scaling exponent of 2 was experimentally observed by Shalchy et al. (2020) for hierarchical porosity in additively manufactured bioengineering scaffolds. Likewise, Chandrasekaran et al. (2021) reported a scaling exponent of 1.81 ± 0.05 for κ-carrageenan aerogels under experimental investigation. Based on the principal mechanisms of linear-elastic deformation (i.e., pore wall bending and axial deformation), Menges and Knipschild (1975) also proposed the relationship between E/E_s and ρ/ρ_s as

$$\frac{E}{E_s} = \frac{C_1(\rho/\rho_s)^2}{\rho/\rho_s + C_2}, \tag{3}$$

with $C_1 = 0.65$ and $C_2 = 0.23$, determined for rigid PUR. Aney et al. (2025) studied the influence of the pore-wall morphology within the framework of Gibson–Ashby open-cell model, showing that particle-neck sizes significantly affect the bulk stiffness. They also highlighted that the scaling exponent depends on the network connectivity: for silica aerogels, an exponent of 3.6 is observed due to the random spatial arrangement of particles and dangling mass, whereas biopolymer or nanofibrous aerogels exhibits an exponent close 2 due to fully interconnected network morphology, reflecting efficient load transfer through the network (Chandrasekaran et al., 2021; Deuber et al., 2017). Further studies by Aney and Rege (2023) and Chandrasekaran et al. (2025) demonstrate the underlying dependence of the effective stiffness on pore-size distribution, in addition to solid fraction or pore-wall thickness, emphasizing the critical role of microstructural heterogeneity in determining the macroscopic mechanical response.

Ashby and Gibson (1997) modeled the plastic yield, elastic buckling, and brittle fracture of cellular structures under multiaxial loading, providing approximate expressions for failure, which were validated against experimental data (Gibson et al., 1989; Triantafillou et al., 1989). They assumed that cracks initiate at the midpoint of the pore wall and propagate discretely along the pore width (Ashby and Gibson, 1997). The fracture toughness of cellular materials is commonly expressed as a function of fracture strength of the pore-wall material (σ_{fs}), relative density (ρ/ρ_s) and pore-wall length. Under tensile loading, pore walls deform elastically in Mode I, transmitting load through

discrete forces and moments. Based on this assumption, Maiti et al. (1984) proposed a relationship between normalized fracture toughness ($K_{IC}/\sigma_{fs}\sqrt{\pi l}$), and relative density using the following power-law:

$$\frac{K_{IC}}{\sigma_{fs}\sqrt{\pi l}} = c\left(\frac{\rho}{\rho_s}\right)^m, \quad \text{with} \quad m = 1.5 \quad \text{and} \quad c = 0.65, \tag{4}$$

where m denotes the scaling exponent and c serves as a proportionality constant. Maiti et al. validated Eq. (4) against the experimental data of commercial polymethacrylimide foams of varying densities, determining $c = 0.65$. Huang and Gibson (1991b) concluded based on finite element study that Eq. (4) is only valid for $d/l < 0.2$ and with crack depth greater than 7 times the pore wall length. Green (1985) derived a correlation similar to Eq. (4), determining $c = 0.28$ and $m = 1.3$ for $0.05 < \rho/\rho_s < 0.30$. Choi and Lakes (1996) also proposed similar relation between K_{IC} and ρ/ρ_s, with $c = 0.2$ and $m = 1.0$, for tetrakaidecahedron cell. Huang and Gibson (1991b,a) further emphasized two critical assumptions underlying classical models:(i) the crack must be large relative to the cell size, and (ii) the pore-wall fracture strength is constant. They introduced a reduction factor for effective fracture toughness in the case of short cracks and highlighted the dependence of fracture resistance on the Weibull modulus of the pore-wall material.

In addition to the classical studies, more recent research has broadly expanded the understanding of fracture in open-porous cellular-like materials (Shahbazian and Mirsayar, 2023). Fleck and Qiu (2007) analyzed several 2-d elastic–brittle lattice topologies–including triangular, hexagonal honeycomb, and kagome lattices–using finite element models. They demonstrated strong dependence of Mode I fracture toughness on relative density, while the kagome lattice exhibited superior toughness. Gu et al. (2018) experimentally showed that the fracture toughness and crack path in 2-d triangular lattices depend on the loading direction. Mirsayar (2022) investigated mixed-mode brittle fracture in 2-d periodic lattices fabricated using additive manufacturing, incorporating material anisotropy associated with build orientation, and proposed a continuum-based fracture criteria to predict crack initiation and propagation. Chen et al. (2022) numerically analyzed fracture trajectories in brittle porous solids with different relative densities under various mixed-mode loading conditions, using a phase-field theory combined with 2-d Voronoi-based model for brittle fracture. Accordingly, in low-density materials, crack paths are governed by weak links in the microstructure and therefore appear stochastic. In contrast, materials with higher densities behave more like continuous solids, where crack trajectories are predominantly controlled by the remote global load. Several studies have also examined fracture in 3-d architected structures, particularly truss-based lattices, relevant to different engineering applications. O'Masta et al. (2017) studied the fracture behavior of 3-d octet-truss lattice structures and showed that the fracture toughness increases linearly with relative density and the square root of the cell size. Gu et al. (2019) also evaluated brittle fracture of 3-d octet-truss lattices with straight and curved cracks, and reported strong dependence of fracture toughness on the orientation and size of the crack. Their findings further confirmed that linear elastic fracture mechanics (LEFM) is valid only for straight (linear) cracks and is not suitable for predicting fracture behavior in lattices with curved cracks. Wei et al. (2018) experimentally and numerically characterized 3-d Kagome lattices produced via selective laser melting, while Xu et al. (2019) studied the influence of printing-direction on deformation and fracture in additively manufactured lattices. At smaller length scales, Patil et al. (2020) analyzed the fracture behavior of graphene aerogels using molecular dynamics and reported that fracture strength decreases with increasing crack length-to-height ratio at the onset of crack propagation, following a power-law dependence on density with a scaling exponent of 1.41 ± 0.04. For silica aerogels, Patil et al. (2018) reported scaling exponents of 2.02 ± 0.05 for Mode I fracture toughness and 1.16 ± 0.04 for strain energy release rate, while Phalippou et al. (1989) experimentally observed an exponent of 1.6 ± 0.2 for fracture toughness using single edge notched beam tests in three point bending. These recent studies collectively underline the increasing research emphasis on fracture phenomena in open-porous materials and highlight the need for systematic modeling frameworks capable of capturing the combined effects of heterogeneous pore morphology, relative density, and crack characteristics–gaps that the present work aims to address.

Analyzing cellular materials under different loading conditions often requires significant computational effort. To reduce this effort, homogenization methods are commonly used, where the heterogeneous structure is replaced by a homogeneous equivalent medium (HEM) (Iltchev et al., 2015; Somnic and Jo, 2022). In this approach, the properties of the material are estimated by analyzing a small representative model, called the representative volume element (RVE) (Hill, 1963). Several homogenization techniques have been developed for cellular materials, including beam theory (Ashby and Gibson, 1997; Cartraud and Messager, 2006; Gibson and Ashby, 1982), asymptotic homogenization (Craster et al., 2010), micropolar theory (Dos Reis and Ganghoffer, 2012), strain energy equivalence (Gad and Gao, 2021; Staszak et al., 2021), multiscale methods (Vigliotti and Pasini, 2012), constitutive modeling (Rege et al., 2016; Rege, 2021) and more recently, machine learning approaches (Bishara et al., 2023; Klawonn et al., 2025). Despite the recent advances, most prior studies have focused on structures with idealiZed or uniform pore morphology (i.e., shape and size) (Thiyagasundaram et al., 2011; Linul and Marsavina, 2011; Linul et al., 2018; Jelitto and Schneider, 2018). To address this limitation, Chandrasekaran et al. (2021) advanced this field of reconstructing 3-d pore morphology of biopolymer aerogel using Laguerre-Voronoi tessellation (LVT) based on a random closed packing of polydisperse spheres (RCPPS). This modeling framework exhibits a power-law dependence of the macroscopic stiffness on the solid fraction under compression, consistent with Eq. (2). Recently, the model was applied to study inelastic effects under large deformations in open-porous cellular materials and was validated against the experimental results from polymeric and metallic foams as well as aerogels (Chandrasekaran et al., 2025). The modeling approach was also recently extended by means of a network decomposition concept to study the solid and gaseous thermal conductivity in such materials (Aney and Rege, 2025). The recent studies demonstrate the effectiveness of this modeling approach in capturing the behavior of open-porous materials, and based on these insights the present study investigates the fracture behavior of open-porous materials with heterogeneous pore shapes and sizes, with high porosity (i.e., $\phi \geq 0.9$). Using computational modeling with LVT and RCPPS, scaling relationships and predictive models are established to provide deeper insights into optimizing next-generation open-porous materials for advanced engineering applications.

2. Methods

An open-porous microstructure with a random PSD can be accurately modeled using a combination of RCPPS and LVT, as demonstrated and validated by Chandrasekaran et al. (2021). The RCPPS method facilitates precise control over the microstructure to achieve a targeted PSD, while the LVT algorithm constructs a network of fully interconnected pore walls enclosing the pore space defined by the RCPPS configuration. This combined approach enables the computational generation of open-porous microstructures with customizable PSDs and solid fractions. In this study, a series of such microstructures were generated using PSDs derived from the probability density function (PDF) of a prescribed distribution, using the following expression,

$$P(D_i) = \frac{f_1(D_i)f_2(D_i)}{\sum_{j=1}^{n} f_1(D_j)f_2(D_j)}, \tag{5}$$

where $P(D_i)$ denotes the PSD associated with each pore-size D_i with $i = 1, 2, 3, \ldots, n$, and n being the number of pore-size intervals. The function, f_1 describes the volume of the pore model (e.g., spherical or cylindrical pores) and f_2 represents the chosen statistical PDF (e.g., normal, beta

Table 1
Material properties of the pore-wall.

Skeletal density (ρ_s)	1200 kg/m^3
Young's modulus (E_s)	3600 MPa
Fracture strength (σ_{fs})	360 MPa

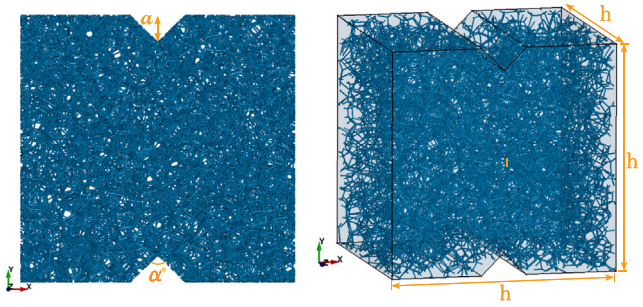

Fig. 1. Double-notched microstructure.

or log-normal). A detailed description of the methodology is provided in Chandrasekaran et al. (2025). In the present study, a spherical pore model combined with a normal distribution is used consistently for all generated microstructures.

A finite element (FE) analysis was performed to investigate the effects of microstructural properties and crack types on fracture behavior. The microstructure generated using LVT was transformed into a cube-shaped representative volume element (RVE) with periodic boundary conditions (PBCs). The FE model of the notched microstructure is illustrated in Fig. 1. Pore walls were discretized using Hughes–Liu corotational beam formulation, which supports large displacements and rotations within an updated Lagrangian framework. This formulation is well suited for bending-dominated pore-wall kinematics in open-porous materials, where large geometric rotations occur even when local beam strains remain small. The pore-wall length and diameter vary within each pore due to the irregular topology of the microstructure. To take it into account, each pore-wall was meshed such that the element aspect ratio (diameter-to-length) remained close to unity, thereby minimizing mesh-size sensitivity and ensuring a reliable structural response. Beam-to-beam interactions were captured using automatic general contact algorithm in LS-DYNA. This approach modeling the macroscopic response of open-porous networks under large compressive strains has been validated in our previous study (Chandrasekaran et al., 2025).

The pore-wall behavior was modeled using a linear isotropic elastic material model characterized by the elastic modulus (E_s) and fracture strength (σ_{fs}). The material properties of polymethacrylimide, reported by Maiti et al. (1984), were adopted to describe the mechanical behavior of the pore walls in the generated microstructures and are summarized in Table 1. Open-porous cellular solids do not fail solely due to principal tensile stress acting on an individual pore-wall; instead, the pore walls experience bending, rotation, axial loading, and shear simultaneously, resulting in a highly multiaxial stress state. For this reason, the von Mises equivalent stress is used as a surrogate measure of the combined stress state within each pore-wall (Lim et al., 2008). Consequently, brittle failure was simulated using element erosion triggered by the von Mises stress criterion.

To evaluate fracture behavior, double-notched microstructures with varying notch (crack) parameters, such as crack depth a and crack angle $\alpha°$ (as shown in Fig. 1), were subjected to tensile loading applied perpendicular to the crack direction, corresponding to Mode I (i.e., opening mode) loading. The simulations were performed using LS-DYNA implicit solver (version R13.0). In this study, we focus on predicting the Mode I fracture toughness and strain–energy release rate using LEFM, which is strictly valid for linear cracks (Gu et al., 2019). Fracture is initiated when the critical stress of the pore walls σ_{fs} is reached, leading to sudden rupture. K_I is called the stress intensity factor, which is the crack driving force, and its critical value, known as fracture toughness (K_{IC}), is a material property that quantifies the resistance to crack extension. The general form of K_{IC} for the opening mode I is given by Chen (1994) as

$$K_{IC} = F_I \sigma_f \sqrt{\pi} a^{p_1}, \tag{6}$$

where σ_f denotes the critical stress at fracture and F_I serves as the dimensionless geometric correction factor of Mode I loading. The parameter $p_1 = 1 - \lambda_1$, with λ_1 being the notch singularity exponent and approximated by Lou et al. (2020) using a simplified closed-form equation:

$$\lambda_1 \approx 0.5 \left[1 + \left(\frac{\alpha°}{180°}\right)^{3.6}\right]. \tag{7}$$

The correction function F_I is defined as a product of the specimen width factor (F_W) and the crack shape factor (F_N), according to Lou et al. (2020), and is expressed as,

$$F_I = F_W F_N, \tag{8}$$

where

$$F_W = \frac{F(a/h)}{1.1215} \tag{9}$$

with

$$F(a/h) = \left(1 + 0.122 \cos^4 \frac{\pi a}{h}\right) \sqrt{\frac{h}{\pi a} \tan \frac{\pi a}{h}}, \tag{10}$$

and

$$F_N = \sqrt{2} + 5.0576 p_1 - 23.027 (p_1)^2 + 41.218 (p_1)^3 - 35.472 (p_1)^4, \tag{11}$$

where a/h represents the crack depth-to-height ratio.

Table 2
Numerical values of F_N for different $\alpha°$ (Savruk and Kazberuk, 2017).

$\alpha°$	0°	30°	60°	90°	120°	150°
F_N	1.1215	1.133	1.186	1.3081	1.515	1.753

Using the numerical values of F_N for different α as provided in Table 2 (Savruk and Kazberuk, 2017, 2007), F_I was calculated for different a/h and α and plotted in Fig. 2(a). Additionally, Eq. (10) is compared to empirical correction functions proposed by Brown (1966) and Benthem and Koiter (1973), with $F_N = 1$ (i.e., excluding the crack angle dependence) in Fig. 2(a). Among these models, the formulation by Tada et al. (1973) demonstrates the highest accuracy, achieving a deviation of only 0.5% across the entire range of a/h (Lou et al., 2020). Consequently, this formulation is used in this study. In contrast, the empirical functions proposed by Brown (for $a/h < 0.35$) and Benthem (for any a/h) exhibit deviation up to approximately 2% (Tada et al., 1973).

According to the fundamental principles of fracture mechanics, the growth of a crack in a stressed plate leads to a reduction in the system's potential energy, while simultaneously increasing the surface energy (Griffith, 1921). The decrease in potential energy is associated with the release of stored energy and the work done by external loads. On the other hand, the increase in surface energy is due to the creation of new crack surfaces, where the atoms are in a non-equilibrium state. Therefore, the surface energy (γ_s) is given by Perez (2004) as

$$\gamma_s = \frac{1}{2}\left(\frac{F_I \sigma_f^2 \pi a}{E}\right). \tag{12}$$

When the strain–energy release rate (G) exceeds the fracture toughness, rapid crack growth occurs. Griffith's energy balance for brittle fracture assumes that external and internal energies are entirely converted into surface energy, neglecting dissipation and kinetic energy (Griffith,

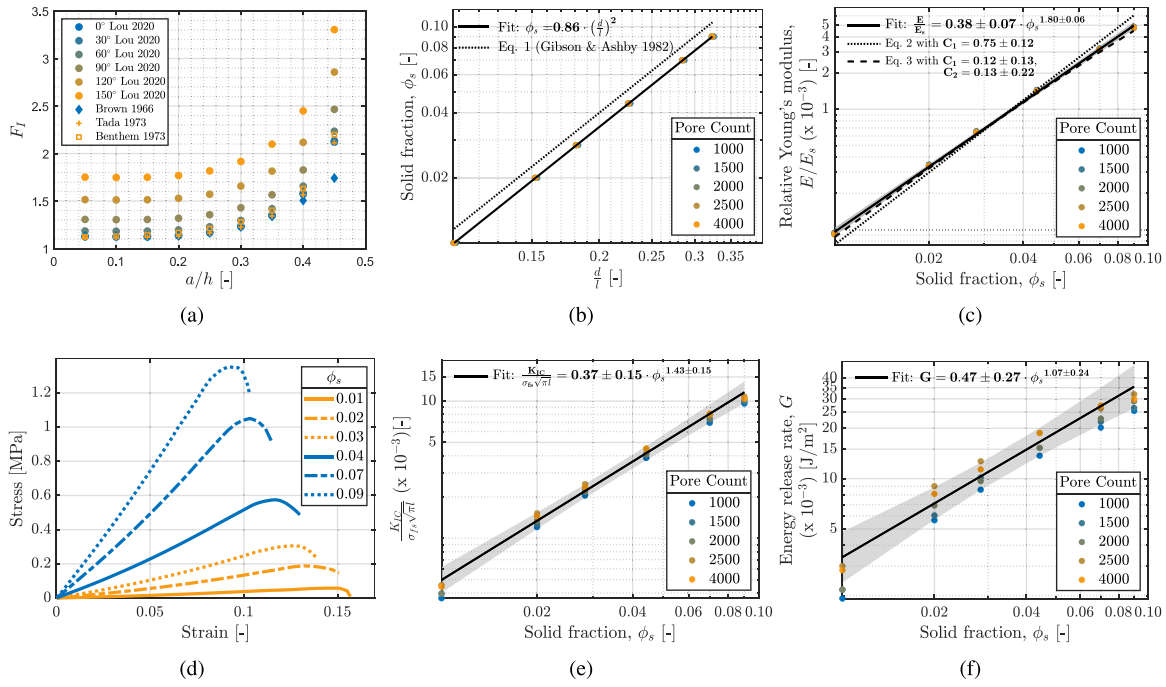

Fig. 2. (a) Comparison of geometric correction function (F_I) calculated using various empirical functions for different a/h and α. Relations identified for unnotched microstructure having different pore counts: (b) ϕ_s vs. d/l and (c) E vs. ϕ_s under tension, plotted on a log–log scale. (d) Stress–strain response of microstructure with different ϕ_s and having a crack with $a/h = 0.2$ & $\alpha = 0°$ subjected to tension, and corresponding fracture properties: (e) $\frac{K_{IC}}{\sigma_{fs}\sqrt{\pi l}}$ and (f) G plotted against ϕ_s in log–log scale.

1921), expressed as $G = 2\gamma_s$. Herein, G can be related to K_{IC} by combining Eqs. (6) and (12), as follows

$$G = 2\gamma_s = a^{(1-2p_1)}\frac{K_{IC}^2}{E}. \tag{13}$$

For $\alpha = 0°$, we get $G = K_{IC}^2/E$, with $p_1 = 0.5$ using Eq. (7).

3. Results and discussion

The representativeness of the RVE with respect to the number of pores was examined in a previous study (Chandrasekaran et al., 2025), which concluded that reliable prediction of geometric and mechanical properties can be achieved as long as the full PSD is adequately captured, regardless of the total pore count. Accordingly, the present study investigates the variation in the elastic modulus of unnotched and the fracture properties of double-notched microstructures under tensile loading across different pore counts. To this end, microstructures were generated using a normal distribution with a mean pore diameter μ = 30 nm and standard deviation $s = 7$, resulting in RVE sizes of 255 nm, 292 nm, 322 nm, 346 nm, and 400 nm for pore counts of N = 1000, 1500, 2000, 2500 and 4000, respectively. The results in Fig. 2 show the representativeness of the RVE, and therefore the minimal size of the RVE was used further in this study, for computational efficiency. Despite variations in pore count and RVE size, all microstructures exhibit a similar average pore-wall length of $l = 11.580 \pm 0.065$ nm. Pore-wall diameters were computed following a diameter-distribution approach for different ϕ_s as outlined by Chandrasekaran et al. (2025). Fig. 2(b) depicts the relationship between ϕ_s and the average d/l ratio for microstructures with varying pore counts. The results indicate that the average d/l ratio across microstructure with different pore counts remains consistent for any given ϕ_s. A quadratic relationship between ϕ_s and d/l is expressed as

$$\phi_s = D\left(\frac{d}{l}\right)^2, \quad \text{with} \quad D = 0.86. \tag{14}$$

A similar relation was proposed by Gibson and Ashby (1982) for 3-d square-shaped cellular structures, with $D \approx 1$ (Oliveira, 2005). Choi and Lakes (1996) reported $D = 1.06$ for a regular tetrakaidecahedron cell, while this study exhibits $D = 0.86$ for a highly heterogeneous microstructure. On the other hand, the scaling exponent of 2 remains consistent, irrespective of the pore shape. The elastic properties of unnotched microstructures were evaluated under tensile loading, with E/E_s plotted against ϕ_s (using E_s = 3600 MPa) in Fig. 2(c). The findings reveal that the elastic response remains unaffected by the pore count across the entire range of ϕ_s. The relationship between E/E_s and ϕ_s adheres to a power-law relationship, as expressed in Eq. (2), with coefficients $C_1 = 0.38$ and $n = 1.8$. The observed scaling exponent aligns closely with $n = 2$, as proposed by Gibson and Ashby (1982). For Eq. (2), $n = 2$ and $C_1 = 0.75$ are identified in this study for widely dispersed pore sizes and shapes. Moreover, Eq. (3), with $C_1 = 0.12$ and $C_2 = 0.13$, demonstrates a strong correlation with the results obtained in this study. The fracture behavior of microstructures, incorporating double-notched cracks with $a/h = 0.2$ and $\alpha = 0°$, was investigated under tensile loading. Stress–strain responses for microstructures with 4000 pores, evaluated for various ϕ_s are presented in Fig. 2(d). It is observed that the fracture stress increases with ϕ_s, while the strain at fracture decreases. An increase in solid fraction results in larger pore-wall diameters, exhibiting higher axial load bearing capacity and bending resistance, thereby contributing to an increased fracture strength. However, these thicker pore-walls tend to reach their maximum fracture strength at lower strain levels. Figs. 2(e) & (f) illustrate the $K_{IC}/\sigma_{fs}\sqrt{\pi l}$ (with σ_{fs} = 360 MPa), and G as functions of ϕ_s, respectively. The normalized fracture toughness follows a power-law relation, as described in Eq. (4), with parameters $c = 0.37 \pm 0.15$ and $m = 1.43 \pm 0.15$. This scaling exponent is approximately equal to the theoretical value of $m = 1.5$ proposed by Maiti et al. (1984). A linear relation between G and ϕ_s is observed by substituting Eqs. (2) & (4) in Eq. (13), as formulated in Eq. (16). Similarly, G demonstrates an approximately linear dependence on ϕ_s, with $c_1 \approx 0.5$ and $m_1 = 1.07$ in the present study.

$$G = a^{(1-2p_1)}\frac{c^2\sigma_f^2\pi l}{C_1 E_s}\phi_s, \tag{15}$$

Table 3
l & d for different ϕ_s and s.

s	l	d [nm]						
	[nm]	$\phi_s =$ 0.01	0.015	0.02	0.03	0.05	0.07	0.1
0.65	14.67	1.56	1.91	2.20	2.70	3.49	4.12	4.93
3.5	14.70	1.57	1.93	2.23	2.73	3.52	4.17	4.98
7	15.22	1.62	1.99	2.29	2.81	3.63	4.29	5.13
14	16.38	1.79	2.19	2.53	3.10	4.00	4.73	5.66
21	18.18	2.02	2.48	2.86	3.50	4.52	5.35	6.39

$$\Rightarrow G = c_1 \phi_s^{m_1} \quad \text{with} \quad m_1 = 1.0. \tag{16}$$

Slight variations in $K_{IC}/\sigma_{fs}\sqrt{\pi l}$ and G, observed across microstructures with different pore counts, lie within the 95% confidence interval of the fitted functions. These results demonstrate that the RVE accurately captures microstructural properties and thus confirm the reliability of the proposed model in predicting the macroscopic Young modulus and fracture properties in open-porous microstructures. The study establishes a robust framework for further investigations into the effect of microstructure and crack configurations on fracture behavior.

3.1. Influence of PSD

In this section, the geometric (d/l), mechanical (E/E_s), and fracture (K_{IC} & G) properties of microstructures with different PSDs are analyzed. This is achieved by varying the coefficient of variation (CV= s/μ), specifically the parameters (μ and s) of the normal distribution. All structures are generated with double notches having $a/h = 0.2$ and $\alpha = 0°$.

3.1.1. Variation in s

Microstructures are generated using the normal distribution with $\mu = 40$ nm and varying $s = 0.65, 3.5, 7, 14$ and 21. The average length of the microstructure and the average pore-wall diameter for different ϕ_s are summarized in Table 3 for different values of s. Although l and d increase with s, the average d/l ratio of these microstructures remains consistent for different ϕ_s. The dependence of ϕ_s on d/l ratio follows a scaling law (as in Eq. (14)) with $D = 0.86 \pm 0.05$ and a scaling exponent of 2.0. Unnotched microstructures exhibit a similar relationship between E/E_s and ϕ_s for varying s, as described in Eq. (2) with $C_1 = 0.37 \pm 0.03$ and $n = 1.80 \pm 0.03$.

In Figs. 3(a) & (b), $K_{IC}/\sigma_{fs}\sqrt{\pi l}$ and G are plotted versus the solid fraction ϕ_s for varying s, following Eqs. (4) and (16), respectively. The constants c, m, c_1, and m_1 associated with these equations decrease with increasing s, as reported in Table 4. As seen in Fig. 3(b), for $\phi_s = 0.01$, the value of G deviates below the fitting function, while for $\phi_s > 0.01$, it aligns well with the proposed relationship. It is observed that G increases with increasing s, which can be attributed to the uniformity of the pore sizes. For lower s, the pores are nearly uniform, resulting in a more homogeneous load distribution among the pore walls. Consequently, fracture initiation is more controlled (Chen et al., 2022), leading to a lower strain energy release per unit crack growth. In contrast, for higher s, the pore sizes vary significantly, producing pore walls lengths and thicknesses with high variation. This heterogeneity creates weaker, highly stressed regions, allowing cracks to propagate more easily along these paths and resulting in a higher strain energy release per crack extension.

3.1.2. Variation in μ

The microstructures are generated using the normal distribution with a variation of $\mu = 20, 30, 40, 50$ nm and a constant $s = 7$. The corresponding structural parameters, l and d, for different ϕ_s and μ are presented in Table 5. The dependence of the d/l ratio and E/E_s on ϕ_s remains consistent for varying μ, following Eqs. (1) & (2), respectively. In Figs. 3(c); (d) & (e), $K_{IC}/\sigma_{fs}\sqrt{\pi l}$, G and σ_f & ϵ_f are plotted against

Table 4
Constants in Eqs. (4) & (16), for varying s.

s	c	m	c_1	m_1
0.65	0.34	1.45	0.5030	1.106
3.5	0.31	1.42	0.4203	1.028
7	0.30	1.39	0.4360	0.9770
14	0.25	1.35	0.3213	0.9055
21	0.24	1.32	0.3415	0.8727

Table 5
l & d for different ϕ_s and μ.

μ	l	d [nm]					
	[nm]	$\phi_s =$ 0.01	0.02	0.03	0.05	0.07	0.1
20	8.22	0.89	1.26	1.55	2.00	2.36	2.82
30	11.63	1.25	1.77	2.16	2.79	3.31	3.95
40	15.22	1.62	2.29	2.81	3.63	4.29	5.13
50	18.39	2.00	2.83	3.46	4.47	5.29	6.32

ϕ_s for different μ, respectively. It is observed from the figures that the fracture stress (σ_f) decreases with increasing μ, while G increases. A similar trend is reported for porous ceramics, where larger pores lead to lower fracture stress but higher fracture energy (Yoshida et al., 2008). In the context of fracture mechanics, pores act as inherent flaws, and the characteristic flaw size scales with the pore-size (Woignier et al., 2015). Since each RVE maintains a constant pore count, an increase in μ directly results in a larger RVE volume characterized by larger pores and longer pore walls. These factors increase the effective flaw size and consequently reduce σ_f. Furtherore, crack propagation in porous microstructures is strongly influenced by the spatial distribution of pore size. Several studies report that cracks tend to curve toward and propagate through regions containing the largest pores rather than following a planar path (Jelitto and Schneider, 2018; Zhang and Shen, 2023). Larger pores create weaker local zones, making them preferential targets for crack extension. Simultaneously, the longer pore walls associated with larger pores exhibit increased bending and axial compliance, allowing them to store more elastic strain energy prior to fracture. When the crack propagates, this stored energy is released, contributing to the observed increase in G. Therefore, the increase in G is intrinsically linked to the volume/size of the microstructure. In contrast, the fracture strain shown in Fig. 3(e) does not exhibit a clear trend with variations in μ, which is attributed to the heterogeneous distribution of pore sizes and pore-wall geometries across microstructures.

The experimental data for the normalized fracture-toughness of Polymethacrylimide (PMI-E) foam (Maiti et al., 1984) and Polyurethane (PUR) foams (McIntyre and Anderton, 1979), plotted in Fig. 3(c), were taken from Jelitto and Schneider (2019). These data provide strong validation for the model, which closely reproduces the experimentally observed trends. The micromechanical model proposed by Maiti et al. (1984) and Green (1985) corresponding to Eq. (4) is plotted for comparison in Fig. 3(c). The constants c and m in Eq. (4), and c_1 and m_1 in Eq. (16), for varying μ, are summarized in Table 6. Analysis of the scaling exponents and proportionality constants, provided in Tables 4 & 6 for Eq. (4), reveals that the model proposed by Maiti et al. ($c = 0.65$ & $m = 1.5$) is particularly well suited for microstructure with smaller pore size or standard deviation, representing uniform PSD, while Green's model ($c = 0.28$ & $m = 1.3$) seems to be better suited for microstructure with large pore size or standard deviation, reflecting more broadly dispersed pore sizes.

3.2. Influence of l & d

The influence of pore-wall length and diameter on fracture behavior was examined by generating two distinct microstructural configurations. In the constant diameter configuration, the distribution of l was

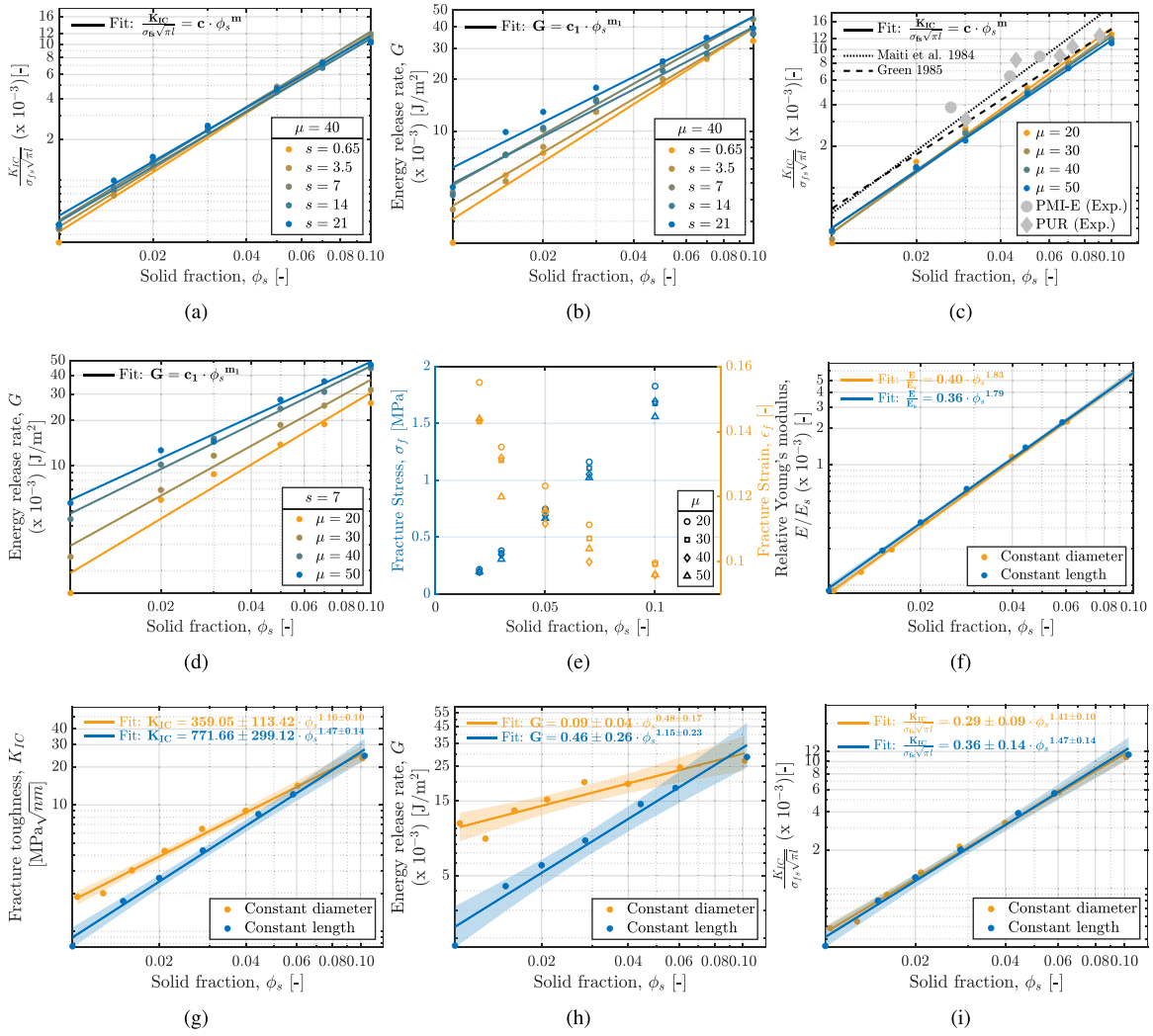

Fig. 3. (a) $K_{IC}/\sigma_{fs}\sqrt{\pi l}$ and (b) G vs. ϕ_s for varying s, (c) $K_{IC}/\sigma_{fs}\sqrt{\pi l}$ and (d) G vs. ϕ_s for varying μ, on a log–log scale, (e) σ_f and ϵ_f vs. ϕ_s for varying μ. Comparison between constant diameter and length configurations for (f) E/E_s, (g) K_{IC}, (h) G and $\frac{K_{IC}}{\sigma_{fs}\sqrt{\pi l}}$ plotted against ϕ_s on a log–log scale.

Table 6
Constants in Eqs. (4) & (16), for varying μ.

μ	c	m	c_1	m_1
20	0.44	1.48	0.48	1.20
30	0.37	1.45	0.47	1.10
40	0.30	1.39	0.44	0.98
50	0.27	1.35	0.41	0.92

Table 7
Structural properties of microstructures with varying l and constant diameter of $d = 4$ nm.

Mean pore Width, μ [nm]	h [nm]	l [nm]	(d/l) [–]	ϕ_s [–]
30	255.28	11.63	0.3476	0.1015
40	332.78	15.22	0.2652	0.0605
50	411.38	18.39	0.2157	0.0399
60	490.73	22.65	0.1766	0.0281
70	570.30	25.87	0.1546	0.0209
80	650.20	29.96	0.1381	0.0161
90	730.20	32.65	0.1225	0.0128
100	810.35	32.65	0.1090	0.0104

varied while keeping d constant across the microstructure. On the other hand, d was varied by maintaining a fixed distribution of l in the constant length configuration. For the **constant diameter** configuration, microstructures with varying mean pore widths were generated. For this purpose, the normal distribution with $\mu = 30, 40, 50, 60, 70, 80, 90$ and 100, and constant $s = 7$ was used to maintain the consistent shape of the PSD for different mean pore widths. Both h and average l increase with μ for a given pore count ($N = 1000$). A constant diameter of $d = 4$ nm was defined for all the pore walls, resulting in variations in ϕ_s of the microstructures. Table 7 summarizes the structural properties, including the mean pore width, RVE size, average pore-wall length, average d/l ratio, and ϕ_s. In the **constant length** configuration, a microstructure was generated based on a normal distribution having $\mu = 30$ and $s = 7$, with $h = 255.28$ nm and average $l = 11.63$ nm. Different values of ϕ_s across the microstructures are obtained by varying d (defined uniformly to all pore walls in the microstructure). Table 8 lists the structural properties for this configuration, including pore-wall diameter d, the average d/l ratio, and the corresponding ϕ_s.

Both configurations exhibit similar dependence of E/E_s on ϕ_s, as illustrated in Fig. 3(f). Fracture analysis was performed using the double-notched microstructures with crack geometries characterized by $a/h = 0.2$ and $\alpha = 0°$. As shown in Fig. 3(g), the power-law scaling exponent between K_{IC} and ϕ_s is lower for the constant diameter configuration compared to the constant length configuration, consistent with previous findings (Choi and Sankar, 2005). A similar trend is observed

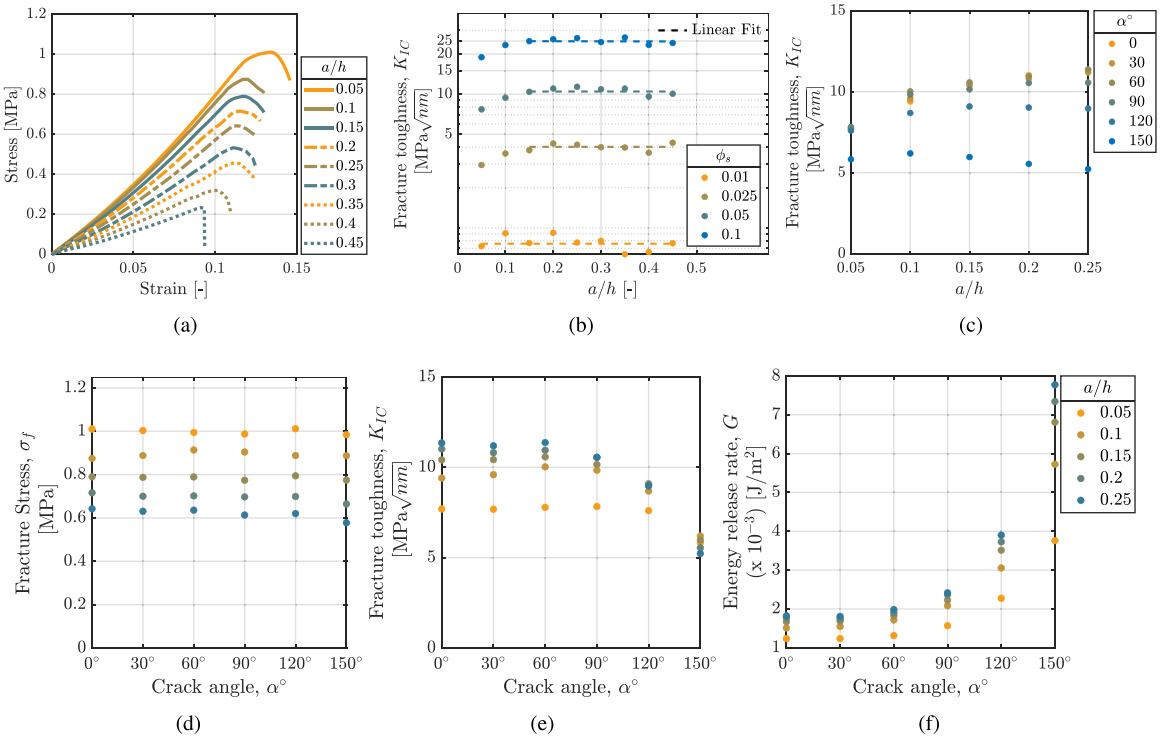

Fig. 4. (a) Stress vs. strain for varying a/h with constant $\phi_s = 0.05$ and (b) K_{IC} plotted against a/h for different ϕ_s, (c) K_{IC} plotted against a/h for different α, Fracture properties: (d) σ_f, (e) K_{IC} and (f) G plotted against α for different a/h, having constant ϕ_s.

Table 8
Structural properties of microstructures with varying d and constant l = 11.63 nm.

ϕ_s [–]	d [nm]	(d/l) [–]
0.0100	1.26	0.1091
0.0150	1.54	0.1336
0.0200	1.76	0.1543
0.0283	2.11	0.1837
0.0442	2.64	0.2293
0.0583	3.03	0.2636
0.1033	4.04	0.3508

in the scaling relationship between G and ϕ_s, as illustrated in Fig. 3(h). However, $K_{IC}/\sigma_{fs}\sqrt{\pi l}$ remains comparable for both configurations, with only slight variation in m, as presented in Fig. 3(i).

Choi and Sankar (2005) reported that K_{IC} is independent of pore size or pore-wall length at low relative density or solid fraction ($0.01 \leq \phi_s \leq 0.04$) and that thicker pore walls yield higher K_{IC} at higher densities. However, Fig. 3(g) demonstrates significant differences in K_{IC} between the two configurations at lower ϕ_s, with these differences diminishing at higher ϕ_s. For instance, at $\phi_s = 0.01$, the constant diameter configuration (characterized by $l = 32.65$ nm and $d = 4$ nm) exhibits a higher K_{IC} than the constant length configuration (with $l = 11.63$ nm and $d = 1.26$ nm). These findings align with Choi et al.'s observations, indicating that pore walls with smaller diameters exhibit reduced fracture strength, leading to lower K_{IC}, independent of ϕ_s. On the other hand, $K_{IC}/\sigma_{fs}\sqrt{\pi l}$ exhibits minimal variation at $\phi_s = 0.01$ compared to K_{IC}, emphasizing the influence of pore-wall length on K_{IC} and G. Pore walls store elastic energy during deformation, which is released during fracture. Consequently, longer and thicker pore walls lead to higher K_{IC} and G. These results highlight the critical role of pore-wall geometry – both diameter and length – in determining the fracture properties of open-porous microstructures. To accurately study the dependence of K_{IC} on ϕ_s, ϕ_s should be varied by adjusting d while maintaining a constitent shape of PSD (i.e., constant length approach) rather than varying the pore-wall length (i.e., constant diameter approach). This is due to the fact that the constant length approach yields a scaling exponent consistent with Eqs. (4) and (16), as inferred from Figs. 3(g) & (h).

3.3. Influence of crack geometry

In this section, the influence of crack configuration, specifically the crack depth-to-height ratio and the crack angle, on the fracture properties is investigated. To this end, microstructures with different crack configurations, based on a PSD described by a normal PDF with $\mu = 30$ and $s = 7$, were generated and subjected to tensile loading. The contour plots presented in Fig. 5 show the resulting von Mises effective stress distribution for different crack configurations, highlighting the predicted crack propagation path through the microstructure.

3.3.1. Effect of a/h

Fig. 4(a) illustrates the stress–strain behavior of microstructures with $\phi_s = 0.05$ and a/h ratios varying between 0.05 and 0.45 while maintaining a constant $\alpha = 0°$ and RVE size. The response is predominantly linear up to the fracture strength, consistent with behavior observed in aerogel and foam materials (Patil et al., 2018; Kabir et al., 2006). As the crack depth increases, the number of effective load-bearing pore walls decreases, leading to a reduction in both the stiffness and fracture strength. For crack depths in the range $0.1 \leq a/h \leq 0.35$, the strain at fracture remains relatively constant as the microstructure still contains sufficient intact pore-walls to redistribute local stresses. Therefore, the crack propagates along a partially tortuous path, allowing some energy dissipation through local bending and stretching of pore walls, which results in similar fracture strain despite reduced strength. In contrast, early fracture is observed for larger cracks, where very few pore walls are available to redistribute stress effectively.

The relationship between K_{IC} and a/h for different $\phi_s = 0.01, 0.025, 0.05$ & 0.1, is depicted in Fig. 4(b). For a highly porous microstructure,

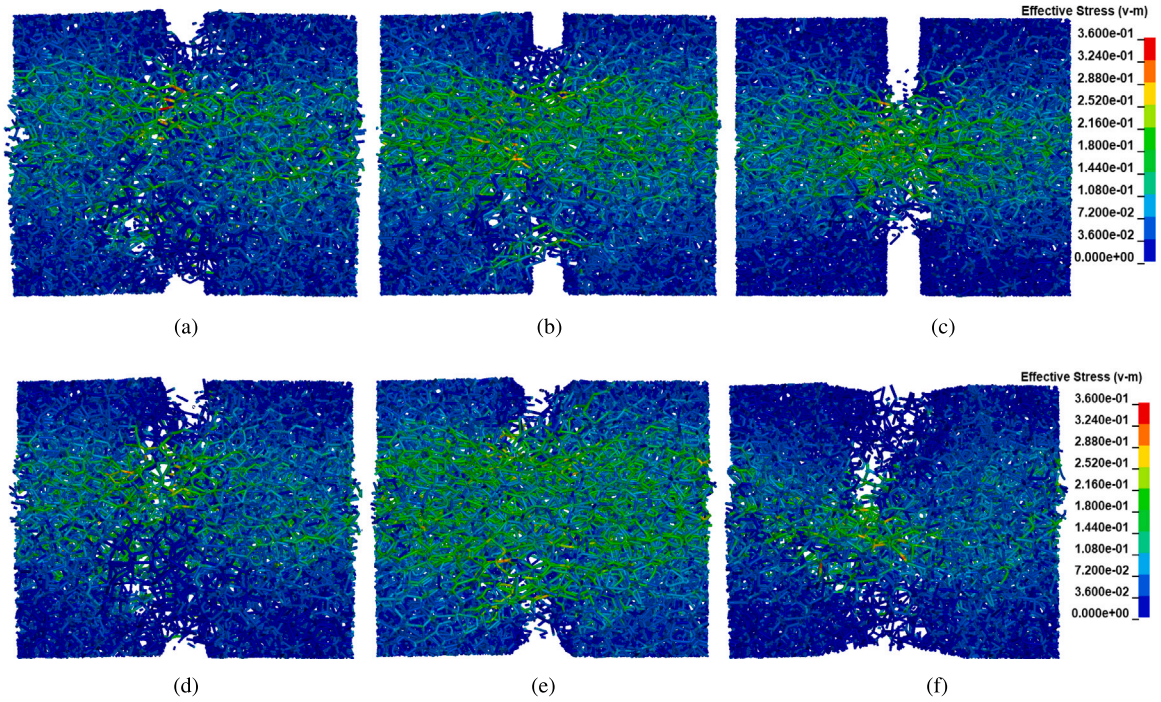

Fig. 5. Crack path in microstructure with $\phi_s = 0.05$ having, $\alpha = 0°$ with (a) $a/h = 0.05$, (b) $a/h = 0.1$ & (c) $a/h = 0.2$, and $a/h = 0.05$ with (d) $\alpha = 30°$, (e) $\alpha = 90°$ & (f) $\alpha = 150°$.

i.e., $\phi_s = 0.01$, the K_{IC} is constant for all a/h values. However, for lower porosity, K_{IC} increases with crack depth for a/h values up to 0.15, consistent with observations in silica aerogels (Patil et al., 2018) and brittle honeycombs (Huang and Gibson, 1991b). However, for a/h values beyond 0.15, K_{IC} stabilizes and exhibits nearly constant magnitude, as illustrated by a linear fit in Fig. 4(b). This behavior aligns with the findings of Choi and Sankar (2005), who reported that fracture toughness is independent of crack depth at higher a/h ratios.

The crack path in the microstructure with crack configurations, $\alpha = 0°$ and $a/h = 0.05,\ 0.1$ and 0.2, is shown in Figs. 5(a), (b) & (c), respectively. For very shallow cracks ($a/h = 0.05$), the crack has minimal influence on the overall load-bearing capacity. The crack path is highly tortuous, forcing interaction with surrounding pore walls, which increases energy dissipation through microcrack deflection and local bending. This leads to higher fracture strength and strain compared to deeper cracks. Whereas, microstructure with $a/h = 0.3$ exhibit a straight crack path, typical of brittle failure, indicating lower fracture strength and strain. All microstructures with $a/h > 0.2$ show fracture behavior with a straight crack path.

3.3.2. Effect of α

The influence of crack angle (varying from 0° to 150°) on fracture stress and toughness, for different $a/h = 0.05,\ 0.1, 0.15, 0.2, 0.25$, is shown in Figs. 4(d) & (e), respectively. It is observed that σ_f is independent of the crack angle for a given a/h ratio, and decreases with increasing a/h. In highly porous microstructures, the effect of crack angle is minimal due to the presence of pores (i.e., inherent flaws) throughout the microstructure (Keleş et al., 2014). The local strength at the crack tip is primarily governed by the geometry of the surrounding pore walls rather than the orientation of the crack itself.

For crack angles $\alpha \leq 60°$, both K_{IC} and G remain nearly constant. This behavior can be attributed to the fact that the crack remains predominantly under Mode I loading, where the applied tensile stress acts perpendicular to the local crack plane. Beyond $\alpha = 90°$, K_{IC} decreases while G increases. This corresponds to a transition from pure Mode I to a mixed-mode fracture, where the crack experiences significant Mode II fracture. This trend is consistent across all a/h values, highlighting that the effect is primarily due to orientation rather than crack size. For a fixed crack angle, K_{IC} and G increase with a/h, as shown in Figs. 4(c) & (f), is consistent with LEFM, where larger cracks result in higher stress intensity factors for the same applied load. The geometric correction function and parameter p_1 account for the influence of crack size, orientation, and specimen geometry, providing a quantitative explanation for the variation of K_{IC} and G even when σ_f remains constant for all angles (refer to Eqs. (11) & (13)). The crack path in the microstructure with crack configurations, $a/h = 0.05$ and $\alpha = 30°,\ 90°$ and 150°, is shown in Figs. 5(d), (e) & (f), respectively. All microstructures show tortuous crack paths, irrespective of crack angle.

4. Conclusion

This study systematically investigates the influence of microstructural features, specifically the PSD and ϕ_s, on the fracture behavior of open-porous materials. RVEs were found to effectively capture the geometric and mechanical characteristics of microstructures across varying pore counts, provided the complete PSD is adequately represented.

The effective Young modulus of the unnotched microstructures exhibits a power-law dependence on ϕ_s, with a scaling exponent $n = 1.8$, closely aligning with the classical theoretical prediction of $n = 2$ (Gibson and Ashby, 1982). The elastic response was found to be unaffected by PSD, while the proportionality constant (C_1) depends on pore structure regularity. In this study, $C_1 \approx 0.38$ was determined for highly heterogeneous pore networks. This relationship can be expressed as

$$\frac{E}{E_s} = C_1 \phi_s^n \quad \text{with} \quad n = 1.80 \pm 0.06. \tag{17}$$

Normalized fracture toughness and strain energy release rate also followed power-law relationships with respect to ϕ_s, as follows

$$\frac{K_{IC}}{\sigma_{fs}\sqrt{\pi l}} \propto \phi_s^m \quad \text{with} \quad m = 1.40 \pm 0.08 \tag{18}$$

and

$$G \propto \phi_s^{m_1} \quad \text{with} \quad m_1 = 1.00 \pm 0.15. \tag{19}$$

Deviations in the scaling exponent m were attributed to PSD variations, highlighting the significant role of PSD in affecting the fracture behavior of open-porous materials having polydisperse pore sizes. A more uniform distribution yields scaling exponents of $m = 1.48$ and $m_1 = 1$, closely matching the theoretical prediction.

The agreement of the model with both the experimental data and the classical scaling relations proposed by Maiti, Gibson, and Ashby for cellular solids (Gibson and Ashby, 1982; Maiti et al., 1984) demonstrates that Voronoi-based microstructures can reliably predict both the elastic and fracture responses under tension. Several observations have been made from this study regarding the fracture behavior of open-porous materials. Variations in the PSD, specifically the standard deviation (s) and mean (μ), were found to significantly influence fracture behavior. Increasing s, which corresponds to more heterogeneous pores, leads to higher strain energy release rates (G) due to stress concentrations at weaker pore walls. Larger mean pore sizes (μ) reduce fracture stress (σ_f) while increasing G, due to large pores acting as inherent flaws. Pore-wall geometry also plays a critical role, with longer and thicker pore walls storing more elastic energy, resulting in higher fracture toughness (K_{IC} and G). Fracture strength and stiffness decrease with increasing crack depth, whereas the fracture stress remains largely insensitive to crack angle, likely because the stress fields are governed primarily by the surrounding pore architecture. However, in the absence of comprehensive experimental studies to substantiate this observation, a detailed investigation into the influence of crack angle on the fracture stress of open-porous materials is required. These findings demonstrate the strong interplay between microstructural features and macroscopic properties and highlight the potential of microstructure-based modeling to predict and optimize the mechanical performance of open-porous materials. A key advantage of the model proposed in this work is that it does not require any parameter fitting: the physical microstructure properties and mechanical properties measured in experiments can be directly used as input to predict the macroscopic response. This modeling framework can also be used to guide the design of microstructural properties before fabricating real materials. Although this study focused on Gaussian PSDs, the model can be extended to non-Gaussian distributions (e.g., beta or bimodal). Preliminary analysis indicates minimal influence of the specific distribution type; thus, only the mean pore size and standard deviation of Gaussian distributions were examined here. The present study also lays the groundwork for integrating advanced machine learning techniques, such as deep symbolic regression, to refine the relationships between microstructure and fracture properties, incorporating the effects of PSD and pore-wall geometry for more efficient and accurate material design.

It is important to note that the present study assumes isotropic behavior of the microstructures; although a heterogeneous PSD is accounted for, the spherical pore-size assumption leads to an effectively isotropic response (Chandrasekaran et al., 2021). Investigation of anisotropic effects, including shear dominated (Mode II) fracture will be addressed in future work. Additionally, the present fracture framework employs linear elastic fracture mechanics, and a linear elastic pore-wall material model is used consistently in this approach. While this is appropriate for capturing the brittle failure at small-strain regime, it does not account for a non-linear mechanical behavior of the pore walls that can arise at large strains. Such non-linearities, including the elasto-plastic pore-wall response under compression reported in our previous study (Chandrasekaran et al., 2025), are therefore beyond the scope of the current work. Incorporating these material-level nonlinear effects in future studies would enable extending the framework to materials where pore-wall yielding or other non-linear deformation mechanisms become relevant, for example in large strain tensile behavior of ductile foams.

CRediT authorship contribution statement

Rajesh Chandrasekaran: Writing – original draft, Visualization, Validation, Software, Resources, Methodology, Investigation, Formal analysis, Data curation, Conceptualization. **Mikhail Itskov:** Writing – review & editing, Supervision, Conceptualization. **Ameya Rege:** Writing – review & editing, Supervision, Formal analysis, Conceptualization.

Declaration of competing interest

The authors declare the following financial interests/personal relationships which may be considered as potential competing interests: Rajesh Chandrasekaran reports a relationship with RWTH Aachen University that includes: employment. If there are other authors, they declare that they have no known competing financial interests or personal relationships that could have appeared to influence the work reported in this paper.

Data availability

Data will be made available on request.

References

Aney, S., Pandit, P., Ratke, L., Milow, B., Rege, A., 2025. On the origin of power-scaling exponents in silica aerogels. J. Sol-Gel Sci. Technol. 114, 98–105.

Aney, S., Rege, A., 2023. The effect of pore sizes on the elastic behaviour of open-porous cellular materials. Math. Mech. Solids 28 (7), 1624–1634.

Aney, S., Rege, A., 2025. Network decomposition model to describe the solid and gaseous thermal conductivity in open-porous (nano) materials. Int. J. Heat Mass Transfer 236, 126316.

Ashby, M.F., Gibson, L.J., 1997. Cellular Solids: Structure and Properties. Press Syndicate of the University of Cambridge, Cambridge, UK, pp. 175–231.

Benthem, J., Koiter, W., 1973. Asymptotic approximations to crack problems. In: Methods of Analysis and Solutions of Crack Problems: Recent Developments in Fracture Mechanics Theory and Methods of Solving Crack Problems. Springer, pp. 131–178.

Bishara, D., Xie, Y., Liu, W.K., Li, S., 2023. A state-of-the-art review on machine learning-based multiscale modeling, simulation, homogenization and design of materials. Arch. Comput. Methods Eng. 30 (1), 191–222.

Brown, Jr., W., 1966. and JE Srawley, ASTM STP 410, vol. 90, Am. Soc. for Test Mat t ls., Philadelphia.

Cartraud, P., Messager, T., 2006. Computational homogenization of periodic beam-like structures. Int. J. Solids Struct. 43 (3–4), 686–696.

Chandrasekaran, R., Hillgärtner, M., Ganesan, K., Milow, B., Itskov, M., Rege, A., 2021. Computational design of biopolymer aerogels and predictive modelling of their nanostructure and mechanical behaviour. Sci. Rep. 11 (1), 10198.

Chandrasekaran, R., Itskov, M., Rege, A., 2025. Influence of microstructure on the mechanical behavior of open-porous materials under large strains. Int. J. Solids Struct. 319, 113441.

Chen, D.-H., 1994. Stress intensity factors for V-notched strip under tension or in-plane bending. Int. J. Fract. 70, 81–97.

Chen, S., Espadas-Escalante, J.J., Isaksson, P., 2022. Numerical analysis of crack path stability in brittle porous materials. Eng. Fract. Mech. 275, 108811.

Choi, J., Lakes, R., 1996. Fracture toughness of re-entrant foam materials with a negative Poisson's ratio: experiment and analysis. Int. J. Fract. 80, 73–83.

Choi, S., Sankar, B.V., 2005. A micromechanical method to predict the fracture toughness of cellular materials. Int. J. Solids Struct. 42 (5–6), 1797–1817.

Craster, R., Kaplunov, J., Postnova, J., 2010. High-frequency asymptotics, homogenisation and localisation for lattices. Q. J. Mech. Appl. Math. 63 (4), 497–519.

Deuber, F., Mousavi, S., Federer, L., Adlhart, C., 2017. Amphiphilic nanofiber-based aerogels for selective liquid absorption from electrospun biopolymers. Adv. Mater. Interfaces 4 (12), 1700065.

Dos Reis, F., Ganghoffer, J.F., 2012. Construction of micropolar continua from the asymptotic homogenization of beam lattices. Comput. Struct. 112, 354–363.

Ensarioglu, C., Bakirci, A., Koluk, H., Cakir, M.C., 2022. Metal foams and their applications in aerospace components. pp. 27–63.

Fleck, N.A., Qiu, X., 2007. The damage tolerance of elastic–brittle, two-dimensional isotropic lattices. J. Mech. Phys. Solids 55 (3), 562–588.

Freyman, T.M., Yannas, I.V., Gibson, L.J., 2001. Cellular materials as porous scaffolds for tissue engineering. Prog. Mater. Sci. 46 (3–4), 273–282.

Gad, A.I., Gao, X.-L., 2021. A generalized strain energy-based homogenization method for 2-D and 3-D cellular materials with and without periodicity constraints. Symmetry 13 (10), 1870.

Gibson, I., Ashby, M.F., 1982. The mechanics of three-dimensional cellular materials. Proc. R. Soc. A 382 (1782), 43–59.
Gibson, L., Ashby, M., Zhang, J., Triantafillou, T., 1989. Failure surfaces for cellular materials under multiaxial loads—I. modelling. Int. J. Mech. Sci. 31 (9), 635–663.
Green, D., 1985. Fabrication and mechanical properties of lightweight ceramics produced by sintering of hollow spheres. J. Am. Ceram. Soc. 68 (7), 403–409.
Griffith, A.A., 1921. VI. The phenomena of rupture and flow in solids. Philos. Trans. R. Soc. Lond. Ser. A 221 (582–593), 163–198.
Gu, H., Pavier, M., Shterenlikht, A., 2018. Experimental study of modulus, strength and toughness of 2D triangular lattices. Int. J. Solids Struct. 152, 207–216.
Gu, H., Shterenlikht, A., Pavier, M., 2019. Brittle fracture of three-dimensional lattice structure. Eng. Fract. Mech. 219, 106598.
Hill, R., 1963. Elastic properties of reinforced solids: some theoretical principles. J. Mech. Phys. Solids 11 (5), 357–372.
Huang, J., Gibson, L.J., 1991a. Fracture toughness of brittle foams. Acta Met. Mater. 39 (7), 1627–1636.
Huang, J., Gibson, L.J., 1991b. Fracture toughness of brittle honeycombs. Acta Met. Mater. 39 (7), 1617–1626.
Iltchev, A., Marcadon, V., Kruch, S., Forest, S., 2015. Computational homogenisation of periodic cellular materials: application to structural modelling. Int. J. Mech. Sci. 93, 240–255.
Jelitto, H., Schneider, G.A., 2018. A geometric model for the fracture toughness of porous materials. Acta Mater. 151, 443–453.
Jelitto, H., Schneider, G.A., 2019. Fracture toughness of porous materials–experimental methods and data. Data Brief 23, 103709.
Kabir, M.E., Saha, M., Jeelani, S., 2006. Tensile and fracture behavior of polymer foams. Mater. Sci. Eng.: A 429 (1–2), 225–235.
Keleş, Ö., García, R.E., Bowman, K.J., 2014. Pore–crack orientation effects on fracture behavior of brittle porous materials. Int. J. Fract. 187 (2), 293–299.
Khan, N.R., Sharmin, T., Rashid, A.B., 2024. Exploring the versatility of aerogels: broad applications in biomedical engineering, astronautics, energy storage, biosensing, and current progress. Heliyon 10 (1).
Kianfar, E., Mahler, A., 2020. Zeolites: properties, applications, modification and selectivity.
Klawonn, A., Lanser, M., Mager, L., Rege, A., 2025. Computational homogenization for aerogel-like polydisperse open-porous materials using neural network-based surrogate models on the microscale. Comput. Mech. 1–21.
Lim, D., Kim, H.S., Kim, Y.H., Kim, Y.H., Al-Hassani, S., 2008. Stress analysis of two-dimensional cellular materials with thick cell struts. J. Mech. Sci. Technol. 22 (5), 835–845.
Linul, E., Marsavina, L., 2011. Prediction of fracture toughness for open cell polyurethane foams by finite-element micromechanical analysis.
Linul, E., Serban, D.A., Marsavina, L., 2018. Influence of cell topology on mode I fracture toughness of cellular structures. Phys. Mesomech. 21, 178–186.
Lou, B., Barltrop, N., Zhang, J., 2020. Geometry parameter method to estimate stress intensity in V-notched plate and a small crack ahead from V-notch apex. Thin-Walled Struct. 154, 106801.
Maiti, S., Ashby, M., Gibson, L., 1984. Fracture toughness of brittle cellular solids. Scr. Metall. 18 (3), 213–217.
McIntyre, A., Anderton, G., 1979. Fracture properties of a rigid polyurethane foam over a range of densities. Polymer 20 (2), 247–253.
Menges, G., Knipschild, F., 1975. Estimation of mechanical properties for rigid polyurethane foams. Polym. Eng. Sci. 15 (8), 623–627.
Mirsayar, M., 2022. On brittle fracture of two-dimensional lattices with material anisotropies. Fatigue Fract. Eng. Mater. Struct. 45 (7), 1929–1941.
Oliveira, F.C., 2005. Elastic moduli of open-cell cordierite foams. J. Non-Cryst. Solids 351 (19–20), 1623–1629.
O'Masta, M.R., Dong, L., St-Pierre, L., Wadley, H., Deshpande, V.S., 2017. The fracture toughness of octet-truss lattices. J. Mech. Phys. Solids 98, 271–289.
Patil, S.P., Rege, A., Itskov, M., Markert, B., 2018. Fracture of silica aerogels: An all-atom simulation study. J. Non-Cryst. Solids 498, 125–129.
Patil, S.P., Shendye, P., Markert, B., 2020. Molecular investigation of mechanical properties and fracture behavior of graphene aerogel. J. Phys. Chem. B 124 (28), 6132–6139.
Perez, N., 2004. Linear Elastic Fracture Mechanics. Springer.
Phalippou, J., Woignier, T., Rogier, R., 1989. Fracture toughness of silica aerogels. Le J. Phys. Colloq. 50 (C4), C4–191.
Rashidi, S., Esfahani, J.A., Karimi, N., 2018. Porous materials in building energy technologies—A review of the applications, modelling and experiments. Renew. Sustain. Energy Rev. 91, 229–247.
Rege, A., 2021. Constitutive modeling of the densification behavior in open-porous cellular solids. Materials 14 (11), 2731.
Rege, A., Schestakow, M., Karadagli, I., Ratke, L., Itskov, M., 2016. Micro-mechanical modelling of cellulose aerogels from molten salt hydrates. Soft Matter 12 (34), 7079–7088.
Savruk, M., Kazberuk, A., 2007. A unified approach to problems of stress concentration near V-shaped notches with sharp and rounded tip. Internat. Appl. Mech. 43, 182–197.
Savruk, M.P., Kazberuk, A., 2017. Stress concentration at notches. Springer.
Shahbazian, B., Mirsayar, M., 2023. Fracture mechanics of cellular structures: past, present, and future directions. Eng. Solid Mech. 11 (2), 231–242.
Shalchy, F., Lovell, C., Bhaskar, A., 2020. Hierarchical porosity in additively manufactured bioengineering scaffolds: Fabrication & characterisation. J. Mech. Behav. Biomed. Mater. 110, 103968.
Somnic, J., Jo, B.W., 2022. Homogenization methods of lattice materials. Encyclopedia 2 (2), 1091–1102.
Staszak, N., Garbowski, T., Szymczak-Graczyk, A., 2021. Solid truss to shell numerical homogenization of prefabricated composite slabs. Materials 14 (15), 4120.
Tada, H., Paris, P.C., Irwin, G.R., 1973. The stress analysis of cracks. Handb. Res. Corp. 34 (1973).
Thiyagasundaram, P., Wang, J., Sankar, B.V., Arakere, N.K., 2011. Fracture toughness of foams with tetrakaidecahedral unit cells using finite element based micromechanics. Eng. Fract. Mech. 78 (6), 1277–1288.
Triantafillou, T., Zhang, J., Shercliff, T., Gibson, L., Ashby, M., 1989. Failure surfaces for cellular materials under multiaxial loads—Ii. comparison of models with experiment. Int. J. Mech. Sci. 31 (9), 665–678.
Twigg, M., Richardson, J., 2002. Theory and applications of ceramic foam catalysts. Chem. Eng. Res. Des. 80 (2), 183–189.
Vigliotti, A., Pasini, D., 2012. Linear multiscale analysis and finite element validation of stretching and bending dominated lattice materials. Mech. Mater. 46, 57–68.
Wei, K., Yang, Q., Ling, B., Xie, H., Qu, Z., Fang, D., 2018. Mechanical responses of titanium 3D kagome lattice structure manufactured by selective laser melting. Extrem. Mech. Lett. 23, 41–48.
Woignier, T., Primera, J., Alaoui, A., Etienne, P., Despestis, F., Calas-Etienne, S., 2015. Mechanical properties and brittle behavior of silica aerogels. Gels 1 (2), 256–275.
Xu, Y., Zhang, H., Šavija, B., Figueiredo, S.C., Schlangen, E., 2019. Deformation and fracture of 3D printed disordered lattice materials: Experiments and modeling. Mater. Des. 162, 143–153.
Yoshida, K., Tsukidate, H., Murakami, A., Miyata, H., 2008. Influence of pore size on fracture strength of porous ceramics. J. Solid Mech. Mater. Eng. 2 (8), 1060–1069.
Zhang, S., Shen, Q., 2023. Effects of pore–crack relative location on crack propagation in porous granite based on the phase-field regularized cohesion model. Materials 16 (23), 7474.
Zhao, S., Malfait, W.J., Guerrero-Alburquerque, N., Koebel, M.M., Nyström, G., 2018. Biopolymer aerogels and foams: Chemistry, properties, and applications. Angew. Chem. Int. Ed. 57 (26), 7580–7608.